Research Square

Preprints are preliminary reports that have not undergone peer review.
They should not be considered conclusive, used to inform clinical practice,
or referenced by the media as validated information.

Ecological Selection Links Cancer Cell Proliferation Dynamics to Phenotypic Plasticity and Drug Resistance

Xuemei Lu

xuemeilu@mail.kiz.ac.cn

Kunming Institute of Zoology, Chinese Academy of Sciences

Lu Yang

Kunming Institute of Zoology, Chinese Academy of Sciences

Yecheng Tan

Kunming Institute of Zoology, Chinese Academy of Sciences

Wen-Bin He

Kunming Institute of Zoology, Chinese Academy of Sciences

Can Liu

Kunming Institute of Zoology, Chinese Academy of Sciences

Guanghao Li

Kunming Institute of Zoology, Chinese Academy of Sciences

Zhucheng Jin

Kunming Institute of Zoology, Chinese Academy of Sciences

Yubo Gong

Kunming Institute of Zoology, Chinese Academy of Sciences

Minling Chen

Kunming Institute of Zoology, Chinese Academy of Sciences

Jinghao Peng

Kunming Institute of Zoology, Chinese Academy of Sciences

Hui Liu

Kunming Institute of Zoology, Chinese Academy of Sciences

Jifan Shi

Kunming Institute of Zoology, Chinese Academy of Sciences

Article

Keywords:

Posted Date: November 16th, 2026

DOI: https://doi.org/10.21203/rs.3.rs-11359535/v1

License: This work is licensed under a Creative Commons Attribution 4.0 International License.
Read Full License

Additional Declarations: There is **NO** Competing Interest.

Ecological Selection Links Cancer Cell Proliferation Dynamics to Phenotypic Plasticity and Drug Resistance

Abstract

Phenotypic plasticity enables cancer cells to survive therapeutic stress, yet how population-level selection generates the regulatory heterogeneity underlying this capacity remains unclear. Here, we integrate ecological life-history theory to examine density-dependent selection as a determinant of population dynamics and regulatory diversity. Building on established microevolutionary model of isogenic cancer cell populations selected under sustained low-density and high-density conditions, we propagated these lineages for 50 additional passages. Through longitudinal genomic, transcriptomic, and chromatin accessibility profiling, we mapped their evolutionary dynamics. Low-density selected (LDS) populations exhibited increased generational transcriptional variation and greater tolerance to diverse therapeutic perturbations than high-density selected (HDS) counterparts. Using single-cell transcriptomic data, we applied a quantitative energy-landscape framework to quantify regulatory plasticity from local gene-expression geometry, revealing that LDS populations maintain more flexible regulatory architectures. Consistent with this plasticity, persister-like states in LDS populations were broadly distributed across transcriptional space rather than confined to discrete subpopulations, suggesting that drug tolerance emerges from population-wide regulatory flexibility. Meta-analyses across independent cancer

datasets supported the generality of this density-driven, fast-proliferating plastic state. Our findings demonstrate that density-dependent selection promotes phenotypic plasticity by increasing population-level regulatory heterogeneity, linking life-history strategy to therapeutic resistance in cancer.

Keywords Density-dependent selection; phenotypic plasticity; drug tolerance; cancer evolution; experimental evolution.

Introduction

Phenotypic plasticity, the ability of genetically identical cancer cells to reversibly transition between functional states, is a central feature of tumor adaptation and therapeutic resistance [1]. Through plastic state transitions, cancer cells can adjust proliferation, stress responses, migration, and drug sensitivity without permanent genetic alterations [2,3]. Despite its clinical importance, a fundamental question remains unresolved: how population-level selection shapes the regulatory heterogeneity underlying phenotypic plasticity[2]. Plasticity is often studied in slow-cycling, quiescent, or dormant states, including drug-tolerant persisters (DTPs) [4,5]. However, aggressive tumors can also harbor rapidly proliferating populations with substantial phenotypic flexibility and tolerance to multiple therapeutic agents[6–8]. This contrast suggests that plasticity cannot be understood solely as an intrinsic property of rare, slow-cycling states, but may instead emerge from population-level evolutionary processes that shape regulatory heterogeneity and state flexibility.

To address this possibility, we turn to ecological life-history theory, particularly density-dependent selection[6,9] In natural populations, density-dependent environments impose distinct selective pressures that favor alternative life-history strategies. Low-density conditions generally favor rapid expansion, whereas high-density conditions favor competitive efficiency and stability[10,11]. These contrasting regimes can influence not only average traits but also the phenotypic and regulatory variation maintained within populations. Thus, plasticity need not arise exclusively from acute stress, dormancy, or expansion of pre-existing resistant clones, but may emerge as a population-level property generated by selection for distinct life-history strategies and regulatory architectures.

At the molecular level, ecological selection may be reflected in gene regulatory networks and cell-state organization. Cell density and cell-cell interactions can influence signaling pathways and transcriptional programs governing proliferation, stress responses, migration, and other cellular phenotypes[6,12]. These processes are increasingly understood as continuous and reversible state landscapes rather than discrete phenotypic switches, potentially allowing populations to maintain heterogeneous regulatory states and flexible phenotypic configurations[13,14]. However, how selection reshapes the geometry and flexibility of regulatory state space, and how this plasticity can be quantitatively measured, remains unclear[3,6].

In our previous work, we experimentally implemented this framework by propagating isogenic cancer cell populations under controlled low-density (LD) and high-density

(HD) conditions for 200 days [15]. This selection generated distinct populations exhibiting divergent life-history strategies, characterized by trade-offs among proliferation, density tolerance, and migration capacity. While these populations exhibit stable trade-offs in proliferation and density dependence, their capacity for phenotypic plasticity remains unknown. Here, we propagate LD- and HD-selected populations for additional 50 passages and performed longitudinal genomic, single-cell transcriptomic, and chromatin accessibility profiling. By combining multi-omic profiling with a quantitative energy-landscape framework, we asked whether the ecological selection governs the structure of regulatory state space. Specifically, we investigate the relationship between phenotypic plasticity and distinct population-level life-history strategies, focusing on how proliferation dynamics govern regulatory flexibility. We further examine how these differences shape the distribution of drug-tolerant persister-like states and assess their generality across independent cancer datasets. By integrating ecological theory with single-cell systems biology, this study aims to establish an ecological and quantitative framework in which phenotypic plasticity is understood as an emergent property of population-level regulatory diversity shaped by life-history strategies.

Results

Evolved Fast Life-History Cells Exhibit Generational Transcriptomic Fluctuation.

In our previous study, we subjected a monoclonal HeLa population to long-term selection under contrasting low-density (LD) and high-density (HD) culture regimes for

83 approximately 200 generations, generating populations with divergent life-history
84 strategies (Fig. 1a)[15]. LD selection favored rapid proliferation and enhanced migratory
85 capacity, whereas HD selection favored slower proliferation and increased tolerance
86 to high population density, revealing a trade-off between rapid population expansion
87 and density-dependent persistence. Importantly, these populations originated from the
88 same genetic background, providing a controlled experimental system in which to
89 investigate how distinct life-history strategies shape subsequent phenotypic and
90 regulatory dynamics.
91 In the present study, we used these previously established low-density selected (LDS)
92 and high-density selected (HDS) populations as the starting populations and
93 propagated them for an additional 50 passages under their respective conditions (Fig.
94 1a). We first asked whether the previously established life-history phenotypes
95 remained stable during this extended period. LDS cells consistently exhibited higher
96 proliferation and lower apoptosis under low-density conditions, whereas HDS cells
97 showed greater survival under high-density conditions (Fig. 1b–d). These phenotypes
98 remained largely stable throughout the additional passages, indicating that the
99 contrasting life-history strategies established by long-term density-dependent
100 selection were maintained during subsequent propagation.
101 We next examined whether the persistence of these phenotypic differences was
102 accompanied by continued genomic or transcriptional evolution. Single-nucleotide
103 variant (SNV) and copy-number analyses revealed that both populations reached

relatively stable genomic configurations, with limited additional genomic changes after approximately 10 passages (Fig. 1e, g; Fig. S1). In contrast, their transcriptional dynamics diverged markedly. HDS cells progressively converged toward stable transcriptional states, whereas LDS cells retained greater transcriptional variation across passages (Fig. 1f, h). These observations suggested that, despite similar genomic stability, the two selection regimes maintained fundamentally different modes of regulatory-state dynamics, providing a foundation for investigating the evolution of phenotypic plasticity.

Density-dependent selection uncouples transcriptional dynamics from genomic alteration.

Principal component analysis (PCA) of bulk transcriptomes revealed distinct evolutionary trajectories in LDS and HDS populations across passages (Fig. 2a). HDS cells exhibited a progressive and directional shift toward stable transcriptional states, consistent with gradual canalization under sustained high-density constraints. In contrast, LDS cells followed non-directional and temporally variable trajectories, indicating greater flexibility in regulatory state space.

We next asked whether the divergent adaptive trajectories generated by density-dependent selection were driven primarily by genomic evolution or by changes in regulatory state flexibility (Fig. 2b). Given the high genomic instability characteristic of cancer cells, we hypothesized that transcriptional evolution could arise either through progressive genomic alterations or through regulatory plasticity that enables

125 transcriptional state transitions independent of major genomic changes. Under the
126 former model, transcriptional divergence would be expected to correlate with genomic
127 variation across evolutionary time[16]. Alternatively, weak coupling between genomic
128 and transcriptional trajectories would indicate increased regulatory flexibility.
129 To distinguish between these possibilities, we integrated single-nucleotide variant
130 (SNV) profiles with transcriptomic similarity across passages (Fig. 2c, d). HDS cells
131 exhibited strong coupling between genomic and transcriptional divergence (Pearson r
132 = 0.97, p = 0.0014), indicating that transcriptional states are tightly constrained by
133 genetic variation. In contrast, LDS cells showed weak coupling (Pearson r = 0.48, p =
134 0.34), demonstrating that transcriptional divergence can arise despite minimal
135 genomic differentiation. These findings indicate that density-dependent selection
136 establishes distinct modes of transcriptional evolution: a genomically constrained,
137 canalized regime in HDS cells, and a regulatory-flexible regime in LDS cells. This
138 uncoupling provides a population-level basis for phenotypic plasticity.
139 **Distinct regulatory architectures underlie flexible and stabilized cell states.**
140 The divergent transcriptional dynamics prompted us to examine whether density-
141 dependent selection establishes alternative regulatory architectures. We therefore
142 integrated bulk transcriptomics, and chromatin accessibility analyses to characterize
143 the molecular features underlying these states.
144 EMT scoring [17] revealed that HDS cells preferentially adopt mesenchymal-associated
145 programs, whereas LDS cells retain a more epithelial-like transcriptional state (Fig.

146 3a) . Notably, LDS cells showed enrichment of developmental signaling pathways,
147 including WNT/β-catenin and Notch signaling pathway, consistent with a regulatory
148 configuration permissive to state transitions (Fig. 3b) [18,19]. In contrast, HDS cells were
149 enriched for mTORC1-associated metabolic programs linked to biosynthetic activity
150 and cellular maintenance (Fig. 3b) [20]. Weighted gene co-expression network analysis
151 (WGCNA) [21] further identified distinct regulatory modules, M1 and M2, associated with
152 LDS and HDS populations, respectively (Fig. 3d,e; Table S1). The M1 was enriched
153 for transcriptional regulation and chromatin organization (Fig. 3f; Fig. S2c,d), whereas
154 the M2 was dominated by ribosome biogenesis and metabolic processes (Fig. 3g; Fig.
155 S2c,d). These results suggested that LDS cells maintain flexible, developmentally
156 poised regulatory programs, whereas HDS cells adopt more constrained, functionally
157 specialized states.
158 Chromatin accessibility profiling supported this distinction (Fig. S3). Transcription
159 factor motif enrichment analysis of LDS/HDS-specific accessible chromatin regions
160 revealed distinct epigenetic landscapes (Fig. S3b). LDS cells were enriched for
161 transcription factor motifs associated with pluripotency and cell-state regulation (e.g.
162 NANOG, SOX2, ZIC3, RUNX1, and RUNX2) [22], whereas HDS cells were enriched for
163 lineage stability and stress-response regulators such as AP-2α, AP-2γ, GATA3, HIF-
164 1α, and HIF-2α (Fig. S3c,d) [23].

Plasticity in LDS populations arises from regulatory flexibility rather than increased heterogeneity.

We next asked whether the increased plasticity of LDS cells was associated with increased population heterogeneity. Single-cell RNA sequencing of LDS10 and HDS10 populations revealed two major transcriptional subpopulations in both groups (Fig. 3h; Table S2). Although these subpopulations differed in cell-cycle composition, cell-cycle variation was not the primary determinant of population structure (Fig. 3i; Fig. S4a). Notably, HDS subpopulations exhibited greater differences in cell-cycle distribution (Table S3) and per-cell RNA detection metrics (Fig. S4b, including nFeature_RNA and nCount_RNA), suggesting higher transcriptional compartmentalization and subpopulation divergence within this populations.

To characterize the core transcriptional programs defining these population structures, we applied consensus non-negative matrix factorization (cNMF) [24]. This analysis identified three major gene expression programs: Program 1, enriched for developmental signaling pathways, was uniformly shared across LDS subpopulations, whereas Programs 2 and 3, associated with proteasome activity, ribosome function, and TCA cycle metabolism, were preferentially utilized by HDS subpopulations (Fig. 3k). These results suggest that the elevated plasticity of LDS cells does not arise from pre-existing transcriptional heterogeneity or subpopulation divergence. Instead, plasticity reflects a population-wide capacity for dynamic state transitions enabled by flexible regulatory architectures. Conversely, HDS cells display fixed subpopulation

specialization associated with canalized, lineage-committed programs.

Regulatory landscape geometry reveals increased plasticity in LDS cells.

Existing approaches for evaluating cellular plasticity often rely on predefined lineage markers or inferred state transition trajectories, which may limit their general applicability across different biological systems [25–27]. To enable a quantitative and marker-free comparison of adaptive flexibility, we developed a biophysical framework based on the local geometry of gene-expression landscapes (Fig. 4). For each cell population, we constructed gene–gene correlation networks based on coordinated expression patterns across individual cells (Fig. 4a,b). The local expression neighborhood surrounding each gene was modeled using a multivariate Gaussian distribution, from which an energy landscape was derived to describe the stability and accessibility of transcriptional states. We quantified gene-level plasticity as the minimum principal curvature of the corresponding energy surface (Fig. 4c). Quantitatively, for gene i in group l, the minimum principal curvature is $\mathcal{K}_{\min} = \left(\lambda_{\min}\left(\Sigma_i^{(l)}\right)\right)^{-1} = \frac{1}{\lambda_{max}\left(\Sigma_i^{(l)}\right)}$, and the gene-level plasticity value is defined as $\mathcal{p}_{g_i}^{l} = \ln(1 + \mathcal{K}_{min})$. Thus, the minimum principal curvature summarizes the dominance of the leading local covariance mode. A larger value indicates weaker dominance of a single covariance mode and is interpreted as a less canalized regulatory organization with greater inferred plasticity (Fig. 4d). Parameter selection, robustness analysis, and computational details are described in Methods and Table S7.

Applying this framework to density-selected populations, we found that LDS cells

exhibited significantly higher plasticity than HDS cells (Wilcoxon test, $p < 0.0001$; Fig. 4e), characterized by weaker dominance of a single leading local covariance modes. Consistently, gene regulatory networks in LDS cells displayed elevated interaction entropy, reflecting increased diversity in regulatory configurations.

Genes within highly plastic regulatory networks in LDS cells were enriched for DNA replication and polymerase-related processes, whereas those in HDS cells were associated with metabolic and stress-response pathways (Fig. 4f). Notably, highly plastic genes exhibited heterogeneous activation across individual cells (Fig. S6), suggesting that plasticity arises from dynamic deployment of regulatory programs rather than uniform transcriptional shifts. Together, this geometry-based framework provides a quantitative approach for assessing transcriptional plasticity, revealing that LDS cells maintain greater regulatory flexibility despite exhibiting limited pre-existing subpopulation divergence.

Regulatory flexibility enables distributed emergence of drug-tolerant states.

Having established that density-dependent selection generates distinct plasticity states, we next examined whether these divergent architectures influence responses to therapeutic stress. We treated both populations with three mechanistically distinct drugs, including homoharringtonine (HHT), cisplatin (DDP), and actinomycin D (ActD) (Fig. 5a; Fig. S7a). Although the IC50 values were comparable between LDS and HDS cells (Table S4), LDS cells maintained significantly higher viability under high-dose drug exposure and exhibited reduced apoptosis following treatment (Fig. 5b,c; Fig.

S7b,c), indicating enhanced tolerance to acute therapeutic stress.

Transcriptomic analyses revealed that LDS cells undergo larger and more diverse state transitions following drug exposure, activating distinct programs depending on treatment context (Fig. 5d; Fig. S7d,e). In contrast, HDS cells exhibited more limited transcriptional responses. Consistently, LDS cells exhibited lower apoptosis rates across six additional drugs with diverse mechanisms of action, demonstrating that their enhanced tolerance represents a broad-spectrum, non-genetic adaptive phenotype rather than drug-specific resistance (Fig. S8).

We next investigated whether the distinct regulatory architectures of LDS and HDS populations shape the cellular routes through which persister-like states emerge. Following high-dose HHT exposure and drug withdrawal, we transcriptionally profiled the surviving drug-tolerant persister cells (Fig. 5e). By projecting drug-induced gene signatures onto single-cell transcriptomes, we mapped persister-associated states onto the pre-treatment transcriptional landscape. In LDS populations, persisters emerged from multiple transcriptionally distinct subclusters, each contributing a relatively small fraction of surviving cells (Fig. 5f–h). In contrast, HDS persisters predominantly originated from a limited subset of pre-existing subclusters that contributed a larger proportion of surviving cells. Similar patterns were observed following DDP treatment (Fig. S8), suggesting that LDS and HDS cells access drug-tolerant states through distinct regulatory routes. Consistent with these differences, LDS derived persisters exhibited stronger EMT-associated transitions following

249 treatment, whereas HDS derived persisters showed more limited reprogramming (Fig.
250 5i). These results indicate that LDS cells achieve drug tolerance through distributed,
251 dynamic state transitions, whereas HDS cells rely more heavily on selection of pre-
252 existing resistant states.

253 To determine whether these distinct tolerance strategies shape subsequent long-term
254 resistance evolution, we generated HHT-resistant derivatives through stepwise drug
255 escalation (see Methods). Following identical selection procedures, both LDS and
256 HDS populations acquired stable resistance, with IC50 values increasing by 5.09-fold
257 and 4.90-fold, respectively (Fig. 5j; Table S5). Resistant derivatives converged in
258 morphology, proliferation, and global transcriptional profiles (Fig. S10a–d). However,
259 LD-derived resistant cells maintained lower apoptosis rates under high-dose HHT
260 exposure compared to HD-derived resistant cells (Fig. 5k, l), suggesting that the highly
261 flexible baseline regulatory architecture of LDS cells confers a sustained survival
262 advantage during the acquisition of stable resistance.

263 **Proliferative-plastic transcriptional states are recurrent across diverse cancer**
264 **contexts**

265 Finally, we examined whether the proliferative–plastic state observed in LDS
266 populations is generalizable across cancer systems. To address this, we examined the
267 relationship between proliferation, transcriptional plasticity, and therapeutic
268 persistence using multiple independent single-cell transcriptomic datasets from cancer
269 cell lines and clinical samples (Table S6). We established a unified framework to

quantify proliferative capacity and transcriptional plasticity across datasets, estimating proliferation based on the proportion of cells in G2/S/M cell-cycle states, and calculating plasticity using the energy-surface curvature framework. Using a dataset comprising 45 samples derived from 42 cell lines, including two non-tumor cell line samples and 43 tumor-derived cancer cell samples [28] ,we observed a significant positive correlation between proliferation and plasticity (Pearson $r = 0.399$, $p = 0.00665$; Fig. 6a), indicating that these features frequently co-occur.

We further examined clinical lung cancer samples representing treatment-naïve tumors (TN), residual disease after therapy (RD), and progressive disease (PD)[29]. Compared with TN and PD samples, RD populations exhibited increased transcriptional plasticity and proliferative activity (Fig. 6b,c), consistent with our finding that therapy-surviving populations preferentially occupy adaptive states characterized by both proliferation and regulatory flexibility.

To investigate whether such states emerge dynamically during treatment adaptation, we analyzed longitudinal single-cell transcriptomic data from SUM159PT breast cancer cells following paclitaxel exposure and drug withdrawal [30]. During the drug-free holiday period, a drug-tolerant clone (DTC) population progressively expanded from an initially minor subpopulation (Fig. 6d,e). Similarly, the analyses revealed expansion of drug-tolerant populations characterized by increased plasticity, sustained proliferation, and reduced apoptosis (Fig. 6f–h). Together, these results demonstrate that proliferative and plastic transcriptional states commonly co-exist across diverse

cancer contexts.

Discussion

Our results support a model in which phenotypic plasticity arises from population-level regulatory organization shaped by density-dependent selection. Under low-density selection, cells maintained more flexible regulatory states, reflected in increased temporal transcriptional variation, reduced coupling between genomic and transcriptional trajectories, and greater plasticity in local gene-expression landscape geometry. In contrast, high-density selection promoted more stabilized transcriptional states, characterized by stronger genomic–transcriptional coupling and reduced regulatory flexibility. These findings indicate that phenotypic plasticity is not simply an intrinsic property of individual cells, but instead reflects regulatory architectures shaped by prior selection history. Finally, analyses across independent cancer datasets indicate that transcriptionally plastic states frequently co-occur with proliferative capacity in both experimental and clinical contexts, including residual disease following therapy. These observations suggest that the adaptive state identified here is not restricted to a specific model system, but reflects a more general feature of tumor evolution.

The emergence of increased transcriptional flexibility in LDS cells is consistent with ecological and evolutionary theory. In natural systems, low-density or expansion-phase populations are often subject to repeated demographic filtering, favoring traits that

311 enable rapid growth and adaptive responsiveness, whereas high-density environments
312 promote stabilizing selection and efficient resource utilization [10,6]. This increased
313 regulatory flexibility may further reflect a bet-hedging strategy, in which populations
314 generate phenotypic variability to enhance survival under uncertain condition[31–33].
315 Although our experimental system does not explicitly impose environmental
316 fluctuations, repeated low-density propagation introduces bottleneck–expansion
317 dynamics that may similarly favor cells capable of maintaining regulatory flexibility. In
318 this context, plasticity can be viewed as a population-level strategy that enables
319 distributed adaptive responses, rather than reliance on rare pre-existing resistant cells.

320 Our results further highlight that phenotypic plasticity should be distinguished from
321 population heterogeneity. HDS populations exhibited greater transcriptional
322 heterogeneity, yet these subpopulations were relatively stable and associated with
323 specialized functional programs. In contrast, LDS cells showed more uniform
324 transcriptional states but retained greater capacity for dynamic transitions. This
325 distinction is consistent with observations in microbial systems, where populations can
326 either diversify into stable specialist states or maintain regulatory flexibility to respond
327 to environmental change[31,34,35]. In cancer, these alternative strategies may represent
328 different solutions to maintaining population fitness under distinct selective pressures.

329 A key implication of this work is that evolutionary history shapes the routes through
330 which drug tolerance emerges. Previous studies have proposed both stochastic state

transitions within homogeneous populations and selection of pre-existing resistant subpopulations as mechanisms underlying persister formation[36–38]. Our results suggest that these mechanisms are not mutually exclusive but instead depend on the regulatory architecture established by prior selection. LDS populations generate drug-tolerant cells through distributed transcriptional transitions, whereas HDS populations rely more heavily on a limited set of pre-existing subpopulations. Consistent with the regulatory features described above, these distinct routes arise from differences in landscape organization: flexible, weakly constrained regulatory states enable population-wide transitions, whereas stabilized architectures restrict adaptation to specific pre-existing states.

These findings support an evolutionary view of cancer in which population-level ecological forces, such as density-dependent selection, shape regulatory landscape architecture and thereby influence adaptive potential. Within this framework, tumor cell populations can occupy distinct evolutionary regimes defined by either regulatory flexibility or stabilization, leading to different modes of therapeutic response. Integrating ecological theory with molecular measurements of regulatory states may therefore provide a useful approach for understanding how adaptive capacity emerges during tumor evolution.

Methods

Generation of low-density-adapted and high-density-adapted cell populations

HeLa cells (Cell Bank, Type Culture Collection Committee, Chinese Academy of Sciences) were cultured in DMEM (Thermo Fisher, 12491015) supplemented with 10% fetal bovine serum (Thermo Fisher, 10099141C) and antibiotics (100 μg/mL streptomycin and 100 U/mL penicillin; Thermo Fisher, 15140122) at 37°C in a humidified incubator with 5% CO_2. All cultures were routinely tested and confirmed negative for mycoplasma contamination.

To generate density-adapted populations, a monoclonal HeLa progenitor population was propagated under two distinct long-term culture regimes. For low-density adaptation, cells were seeded at 1 × 10^3 cells/cm² and cultured for 120 h until reaching approximately 5 × 10^3 cells/cm². At each passage, 2–3% of cells were transferred to initiate the next generation. For high-density adaptation, cells were seeded at 1 × 10^5 cells/cm² and cultured for 72 h until reaching approximately 8 × 10^5 cells/cm². At each passage, approximately 50% of cells were retained for subsequent propagation. Both regimes were maintained for 40 passages (~200 days).

Following the initial evolution phase, low-density selected (LDS) and high-density selected (HDS) populations were further propagated under their respective culture conditions. Samples were collected at passages 0, 10, 20, and 50 for whole-genome sequencing (WGS), ATAC-seq, and RNA-seq analyses. An additional LDS sample was

collected at passage 15 for transcriptomic analysis. Passage-10 populations were used for subsequent single-cell RNA sequencing and drug-response experiments.

Cell proliferation assay and growth curve modeling

Cell proliferation dynamics were quantified by seeding 3,000 cells per well in 24-well plates and maintaining cultures in complete DMEM (10% FBS, 1% penicillin/streptomycin) under standard conditions (37 °C, 5% CO_2). Cell numbers were measured every 24 h over a 96 h period using the Countstar Automated Cell Counter (IC1000, ALIT Life Sciences). Proliferation rates (*r*) were estimated by modeling population growth according to the exponential equation (1):

$$\frac{d\boldsymbol{N}(\boldsymbol{t})}{d\boldsymbol{t}} = \boldsymbol{r}\boldsymbol{N}(\boldsymbol{t}) \quad (1)$$

In equation (1), $N(t)$ denotes the cell number at time t, and r represents the proliferation rate. Raw cell counts were $\log_2$-transformed, and proliferation rates were obtained by fitting a linear regression model using the least-squares method. The slope of the regression line was taken as the proliferation rate for each population.

Apoptosis analysis at low/high density culture

To evaluate the adaptability of LDS and HDS cells under low/high density conditions, we analyzed cell apoptosis using the Annexin V-APC/PI Apoptosis Detection Kit (Elabscience Biotechnology Co., Ltd. E-CK-A217). First, cells were seeded in 6-well plates at densities of 2000 cells/cm² (low density) and 40,000 cells/cm² (high density)

and cultured for 72 hours. Subsequently, adherent cells were detached using EDTA-free 0.25% trypsin (ThermoFisher, 15050065) and then both detached cells and suspension cells were collected by centrifugation (2000 rpm, 5 minutes). The collected cells were washed twice with PBS and then resuspended in 500 μL of Binding Buffer. After adding 5 μL each of Annexin V-APC and PI, the samples were incubated at room temperature in the dark for 5–10 minutes and analyzed within 1 hour using a flow cytometer. Annexin V-APC was detected using the FL4 channel (Ex = 633 nm, Em = 660 nm), while PI was detected in the FL3 channel (Ex = 488 nm, Em ≥ 630 nm). Fluorescence compensation was performed using apoptosis-induced control cells.

Cell viability assay under drug treatment

Adherent cells (20,000 cells/ cm^2, 24 h pre-culture) were exposed to culture medium containing different concentrations of chemotherapeutic agents (cisplatin, actinomycin D, or homoharringtonine) for 24 h. To comprehensively evaluate drug-induced cellular responses, cell viability was assessed through two parallel approaches: the CCK-8 assay (APExBIO Co., Ltd. K1018), which measures dehydrogenase activity as an indicator of cytostatic effects, and Annexin V-FITC/PI staining coupled with flow cytometry to quantify apoptotic populations and assess cytotoxic effects. All experiments were conducted with three biological replicates to ensure reproducibility. This dual-method strategy enables simultaneous evaluation of growth inhibition and cell death, providing robust assessment of drug efficacy.

RNA extraction and sequencing

Total RNA was extracted from adherent cells in 6-well plates using the RNeasy Plus Kits for RNA Isolation (Qiagen, 74134). RNA quality was assessed by agarose gel electrophoresis and Nanodrop spectrophotometry (OD260/280 ratio >1.8, OD260/230 >2.0), with integrity further verified using Agilent 2100 Bioanalyzer (RIN ≥7.0). Qualified RNA samples were subjected to library preparation and paired-end 150 bp sequencing on Illumina NovaSeq 6000 platform by Novogene Co., Ltd (Beijing, China), with a minimum sequencing data of 6 Gb per sample.

RNA-seq data processing

Raw sequencing data were quality-controlled and adapter-trimmed using fastp (Ver 0.23.4) [39]. Clean reads were aligned to the reference genome using HISAT2 (Ver 2.2.1) [40] with default parameters. The resulting SAM files were converted to BAM format and sorted using samtools (Ver 2.2.1) [41]. Gene expression quantification was performed using featureCounts to generate read count matrices. The count matrices were subsequently converted to gene symbols and normalized to transcripts per million (TPM) for downstream analysis.

Principal component analysis and calculation of transcriptional differences

Gene expression profiles were subjected to principal component analysis (PCA) using the PCA() function in FactoMineR (v2.11) and R (4.4.3), with data preprocessed by transcripts per million (TPM) transformation and standardization (mean-centered and

scaled to unit variance). The top n principal components (PCs) explaining >85% of the total variance were retained for downstream analysis. To quantify the transcriptional differences between samples, pairwise Euclidean distances between samples were computed based on the selected PCs (derived from the 85% variance cutoff).

Whole genome sequencing library preparation

Genomic DNA was extracted from approximately 30,000 cells cultured for 3 days in 6-well plates using the DNeasy Blood & Tissue Kit (Qiagen, 69504). DNA quality was verified by agarose gel electrophoresis and spectrophotometric analysis (OD260/280 ratio 1.8-2.0). Qualified DNA samples were used for whole genome sequencing library construction and paired-end 150 bp sequencing was performed on the BGI DNBSEQ-T7 platform and roughly 180Gb raw data (~60X coverage) was generated for each sample.

Whole genome sequencing data processing

Raw sequencing data in FASTQ format were processed through a standardized bioinformatics pipeline. Initial quality control and adapter trimming were performed using fastp. Quality-filtered reads were aligned to the human reference genome (hg38) using BWA (v0.7.17) [42] MEM algorithm with default parameters. Read group information was added during alignment. The resulting SAM files were converted to BAM format and sorted using samtools. Duplicate reads were marked using Picard Tools (v2.18.29) MarkDuplicates. Local realignment around known indels was

performed using GATK3 (v3.8-1) RealignerTargetCreator and IndelRealigner tools, with known indel sites from the hg38 reference set. Base quality score recalibration (BQSR) was applied using GATK3 BaseRecalibrator and PrintReads, with dbSNP (v138) as known sites. The final recalibrated BAM files were used for downstream analysis.

Somatic variant calling and SNV phylogenetic analysis

Somatic variant calling was performed using GATK4 Mutect2 with tumor-normal paired analysis mode. The germline resource af-only-gnomad.hg38.vcf.gz was used for contamination estimation. Variants were filtered using FilterMutectCalls with contamination tables generated by CalculateContamination.

For phylogenetic analysis, indels were removed from the filtered VCF files using vcftools (v0.1.16) [43] with parameters: --remove-filtered-all, --remove-indels, --recode, --recode-INFO-all, and --max-alleles 2. Filtered VCF files from multiple samples were merged using bcftools merge (v1.9).

A custom Python script converted the merged VCF to FASTA format by: (1) extracting SNP positions across all samples, (2) constructing concatenated SNV sequences for each sample, and (3) generating both FASTA and genotype matrix outputs. Phylogenetic reconstruction was performed using MEGA12 [44] software with maximum likelihood method and 500 bootstrap replicates. Genetic distances between samples

were calculated using p-distance model.

Copy Number Variation Analysis

With processed BAM files, CNV analysis was performed using Control-FREEC (v11.6b) [45] with the following parameters: ploidy = 2, window size = 50,000 bp, and breakPointThreshold = 0.8. The hg38 reference genome was used with corresponding GC content profile and mappability files for normalization.

CNV Annotation and Integration

The identified CNV regions were annotated using GenomicRanges (v1.56.2) and org.Hs.eg.db (3.19.1) packages in R. Gene overlapping analysis was performed by mapping CNV segments to known genes from the TxDb.Hsapiens.UCSC.hg38.knownGene database..

Assessing the Functional Impact of Copy Number Variations on Gene Expression

To investigate the functional impact of CNVs in module genes, we performed correlation analysis between gene expression levels (log_2 fold change) and the copy number status of their genomic regions. This integrative approach allowed identification of genes whose expression patterns correlated with underlying copy number alterations.

ATAC-seq library preparation

Libraries for ATAC-seq were prepared using the Hyperactive ATAC-Seq Library Prep Kit for Illumina (Vazyme, TD711) according to the manufacturer's protocol. Briefly, 50,000 cells were washed and lysed in ice-cold Lysis Buffer. Nuclei were extracted using TruePrep Tagment Enzyme Mix V50 at 37°C for 30 min. After stopping the reaction, DNA was purified using ATAC DNA Extract Beads and amplified with 2× CAM Master Mix and dual-indexed primers (TruePrep Index Kit, Vazyme) for 12 cycles. Amplified libraries were size-selected using a double-sided bead-based cleanup with ATAC DNA Clean Beads.

Library quality was assessed using the Agilent 2100 Bioanalyzer and quantified by Qubit dsDNA HS Assay (Thermo Fisher Scientific). Sequencing was performed on the Illumina platform by Berry Genomics (Beijing, China) with a paired-end 150 bp read length, generating approximately 12 Gb of data per sample.

Peak calling from ATAC-seq data

Raw paired-end ATAC-seq reads were processed with fastp for quality control and adapter trimming. High-quality reads were aligned to the hg38 genome using Bowtie2 (v2.5.1) [46], followed by removal of mitochondrial reads with SAMtools (v1.17) and PCR duplicates with Picard(v2.27.4) MarkDuplicates. Normalized BigWig files for visualization were generated using deepTools (v3.5.2)) [47] bamCoverage with RPKM normalization. Peak calling was performed with MACS3 (v3.0.0) [48], and replicate

concordance was evaluated using IDR (v2.0.4) at a threshold of 0.05. Data quality, assessed as TSS enrichment score, was assessed with deepTools over a ±2 kb window around GENCODE v39 TSSs, excluding the ENCODE blacklisted regions.

For quantitative comparison, a consensus peak set was constructed by merging all concordant peaks passing IDR threshold using HOMER v5.1 mergePeaks. Read counts per sample were extracted across these consensus regions using deepTools multiBamSummary, followed by normalization to RPKM in R software.

Discovery of Transcription Factor Motifs in LDS/HDS-specific Accessible Regions

Differentially accessible regions (DARs) between LDS and HDS cells were identified using DESeq2 (v1.44.0; $q < 0.01$). De novo motif discovery was performed on the DAR coordinates using HOMER (v5.1) to identify transcription factor motifs enriched in LDS-specific or HDS-specific accessible regions relative to the background genome.

Single-cell RNA sequencing and data analysis

Single-cell libraries were prepared using the 10x Genomics Chromium platform (v3 chemistry) from suspensions with ≥90% viability. Following standard library preparation and quantification, sequencing was performed on an Illumina NovaSeq 6000 (150-bp paired-end). Raw data were processed with the 10x Cell Ranger pipeline. The filtered feature-barcode matrices were analyzed in Seurat (v5.0.2) [49] for quality control,

ambient RNA removal (decontX, v1.2.0) [50], and doublet removal (DoubletFinder, v2.0.4)[51]. The Seurat workflow included normalization, identification of the top 2,000 highly variable features (selection.method = "vst"), scaling, principal component analysis (30 PCs), construction of a shared nearest neighbor graph (top 10 PCs), clustering (resolution = 0.1), and visualization with UMAP (dims = 1:10).

Plasticity estimation from energy landscape stability

Notations. We denote the gene expression matrix as $\boldsymbol{X} \in \mathbb{R}^{n \times p}$, where n is the number of cells and p is the number of genes. Each row $\boldsymbol{x}^{(\mathrm{i})} \in \mathbb{R}^{p}$ represents the gene expression profile of the i-th cell. We assume that the cell population is partitioned into K groups, denoted as $\mathcal{G} = \{G_1, G_2, \ldots, G_K\}$, where each group G_l contains n_l cells and satisfies $\sum_{l=1}^{K} n_l = n$. For each group G_l, we denote the corresponding gene expression matrix as $\boldsymbol{X}_l \in \mathbb{R}^{n_l \times p}$, which contains the expression profiles of all cells in that group.

Gene-gene correlation network construction. For each group G_l, we compute the gene-gene Pearson correlation matrix $C_l \in \mathbb{R}^{p \times p}$ as:

$$C_l = \rho\left(\boldsymbol{X}_l^T\right) \tag{1}$$

where $\rho(\cdot)$ computes the Pearson correlation between genes. Specifically, each entry $[C_l]_{ij}$ represents the Pearson correlation between the expression vectors of genes i and j across all cells in group G_l, as defined in equation (1).

Energy landscape modeling based on local neighborhood. For each gene g_i in group G_l, we define its neighborhood $\mathcal{N}_i^{(l)}$ as:

$$\mathcal{N}_i^{(l)} = \{j \in \{1,2,\dots,p\} \setminus \{i\} \mid \left|[C_l]_{ij}\right| \geq \tau\} \tag{2}$$

Let gene g_i in group G_l have m neighbors, such that $\left|\mathcal{N}_i^{(l)}\right| = m$. Let $g_i^{(l)}$ denote the joint expression vector comprising the focal gene and its m neighbors and assume that it follows a multivariate Gaussian distribution. Before estimating the local covariance structure, the expression matrix of gene g_i and its neighbors is standardized to have zero mean and unit variance across cells. This normalization ensures that each gene contributes equally to the covariance estimation, avoiding bias due to differences in expression scale. Based on the standardized expression profiles across all cells in group G_l, we compute the sample mean vector and sample covariance matrix. Then, the density of of gene $g_i^{(l)}$ is:

$$p\left(\boldsymbol{g}_i^{(l)}\right) = \frac{1}{\sqrt{(2\pi)^{m+1}\det\left(\boldsymbol{\Sigma}_{\mathrm{i}}^{(l)}\right)}} \exp\left(-\frac{1}{2}\left(\boldsymbol{g}_i^{(l)} - \boldsymbol{\mu}_i^{(l)}\right)^{\mathsf{T}}\left(\boldsymbol{\Sigma}_{\mathrm{i}}^{(l)}\right)^{-1}\left(\boldsymbol{g}_i^{(l)} - \boldsymbol{\mu}_i^{(l)}\right)\right) \tag{3}$$

where $\boldsymbol{\mu}_i^{(l)} \in \mathbb{R}^{m+1}$ and $\boldsymbol{\Sigma}_{\mathrm{i}}^{(l)} \in \mathbb{R}^{(m+1)\times(m+1)}$ are estimated using the sample mean vector and sample covariance matrix computed from the expression profiles of gene $\mathrm{g_i}$ and its neighbors across all cells in group G_l.

Based on this probabilistic model, we define the following energy function to quantify the local geometric complexity of gene g_i:

$$E\left(\boldsymbol{g}_i^{(l)}\right) = -\ln p\left(\boldsymbol{g}_i^{(l)}\right) \tag{4}$$

which can be written explicitly as:

$$E\left(\boldsymbol{g}_i^{(l)}\right) = \frac{1}{2}\left(\boldsymbol{g}_i^{(l)} - \boldsymbol{\mu}_i^{(l)}\right)^{\top}\left(\boldsymbol{\Sigma}_{\mathrm{i}}^{(l)}\right)^{-1}\left(\boldsymbol{g}_i^{(l)} - \boldsymbol{\mu}_i^{(l)}\right) + \frac{1}{2}\ln\left[(2\pi)^{m+1}\det\left(\boldsymbol{\Sigma}_{\mathrm{i}}^{(l)}\right)\right] \tag{5}$$

To quantify the plasticity of gene g_i, we examine the local stability of its energy landscape. Specifically, we define gene plasticity using the minimum principal curvature at the origin of the energy surface $E\left(\boldsymbol{g}_i^{(l)}\right)$, which characterizes the least-stable local direction.

Quantifying gene plasticity modeling and aggregating group-level scores. We define the plasticity of gene g_i based on the minimum principal curvature at the origin of this energy surface. The minimum principal curvature quantifies stability along the least-stable local direction. A large value indicates that this weakest direction remains relatively stable and that local variation is less dominated by a single high-variance covariance mode. We interpret this more evenly distributed local stability, rather than instability of the mean state, as reduced regulatory canalization and greater inferred plasticity. Conversely, a smaller value indicates a dominant low-stability mode and a more canalized, less plastic expression pattern.

Since the principal curvatures are equal to the eigenvalues of its Hessian matrix, and the energy function is quadratic in form, we compute the Hessian of $E\left(\boldsymbol{g}_i^{(l)}\right)$ as $\nabla^2 E\left(\boldsymbol{\mu}_i^{(l)}\right) = \left(\boldsymbol{\Sigma}_{\mathrm{i}}^{(l)}\right)^{-1}$. The minimum principal curvature is therefore the smallest eigenvalue of $\left(\boldsymbol{\Sigma}_{\mathrm{i}}^{(l)}\right)^{-1}$, or equivalently, the reciprocal of the largest eigenvalue of $\boldsymbol{\Sigma}_{\mathrm{i}}^{(l)}$:

$$\mathcal{K}_{min} = \left(\lambda_{\min}\left(\boldsymbol{\Sigma}_{\mathrm{i}}^{(l)}\right)\right)^{-1} = \frac{1}{\lambda_{max}\left(\boldsymbol{\Sigma}_{\mathrm{i}}^{(l)}\right)} \tag{6}$$

Thus, we define the plasticity of gene g_i in group G_l as:

$$\mathcal{p}_{g_i}^{l} = \ln(1 + \mathcal{K}_{min}) \tag{7}$$

To obtain a group-level plasticity score, we rank all genes within group G_l by their plasticity scores, and compute the average of the top k genes:

$$\mathcal{p}(G_l) = \frac{1}{k}\sum_{j=1}^{k} \mathcal{p}_{g_{(j)}}^{l} \tag{8}$$

To ensure robustness, each sample was randomly subsampled at 80% of cells and the procedure repeated 100 times. The choice of total gene number p, correlation threshold for partitioning the gene co-expression network and the parameter *k* varied according to sample size, and the final settings are summarized in Supplementary Table 7.

The persister cell isolation

The persister cell isolation experiment was performed as follows: 200,000 cells per well were seeded in 6-well plates and cultured overnight. The medium was then replaced with fresh medium containing compounds/drugs at concentrations that induced ~90% inhibition of cell viability, followed by 48 hours of treatment. After drug exposure, the medium was replaced with normal culture medium. Cells were allowed to recover until they reached 70%–80% confluence, after which total RNA was extracted for transcriptome library construction.

Inference of Persister Cell Origins

To infer the distribution of persister cells that survived drug treatment within the original cell population, we identified marker gene sets comprising the top 500 significantly upregulated genes (Deseq2 $q < 0.01$, ranked by fold change) in persister transcriptome samples compared to the control group. Using the AUCell (ver1.26.0) scoring method, we defined the top 5% of cells with the highest scores as potential persisters. To better visualize and quantify the distribution of these persisters, we clustered the single-cell transcriptome data at a relatively high resolution (resolution = 0.5) and calculated the proportion of persister cells within each resulting cluster.

Generation of HHT-resistant cell lines

LDS and HDS cells were initially treated with 16 ng/mL homoharringtonine (HHT). Following each treatment, the drug-containing medium was replaced with fresh

complete medium, and cells were allowed to recover until reaching approximately 70% confluence. Cells were then passaged overnight before the next round of drug treatment. Each HHT concentration was administered for two consecutive treatment cycles, after which the drug concentration was approximately doubled. This iterative treatment and recovery process was continued until the HHT concentration reached 2,000 ng/mL, at which point the HHT-resistant cell lines were considered established.

Statistical Analyses

All experiments were conducted in triplicate, and the experimental data were expressed as the mean ± standard deviation. Statistical analyses were performed by R and GraphPad Prism8.0 software, with two-sided Wilcoxon or Student's t-test applied for comparison between groups as appropriate. Pearson's correlation analysis was used to evaluate the correlation between variables. A p-value < 0.05 was considered statistically significant.

Reference

1. Hanahan, D. Hallmarks of cancer: New dimensions. *Cancer Discov.* **12**, 31–46 (2022).
2. Torborg, S. R., Li, Z., Chan, J. E. & Tammela, T. Cellular and molecular mechanisms of plasticity in cancer. *Trends Cancer* **8**, 735–746 (2022).
3. Pantina, V. D. *et al.* Evolutionary insights into tumor progression: integrating genetic mutations and phenotypic plasticity. *Mol. Cancer*

https://doi.org/10.1186/s12943-026-02770-y (2026) doi:10.1186/s12943-026-02770-y.

4. Marsolier, J. *et al.* H3K27me3 conditions chemotolerance in triple-negative breast cancer. *Nat. Genet.* **54**, 459–468 (2022).
5. Sharma, S. V. *et al.* A chromatin-mediated reversible drug-tolerant state in cancer cell subpopulations. *Cell* **141**, 69–80 (2010).
6. Aktipis, C. A., Boddy, A. M., Gatenby, R. A., Brown, J. S. & Maley, C. C. Life history trade-offs in cancer evolution. *Nat. Rev. Cancer* **13**, 883–892 (2013).
7. Rehman, S. K. *et al.* Colorectal Cancer Cells Enter a Diapause-like DTP State to Survive Chemotherapy. *Cell* **184**, 226-242.e21 (2021).
8. Rezayatmand, H., Razmkhah, M. & Razeghian-Jahromi, I. Drug resistance in cancer therapy: the Pandora's Box of cancer stem cells. *Stem Cell Res. Ther.* **13**, 181 (2022).
9. Stearns, S. C. Trade-offs in life-history evolution. *Funct. Ecol.* **3**, 259–268 (1989).
10. Reznick, D., Bryant, M. J. & Bashey, F. r- and K-Selection Revisited: The Role of Population Regulation in Life-History Evolution. *Ecology* **83**, 1509–1520 (2002).
11. Travis, J., Bassar, R. D., Coulson, T., Reznick, D. & Walsh, M. Density-Dependent Selection. *Annu. Rev. Ecol. Evol. Syst.* **54**, 85–105 (2023).
12. Sharif, G. M. *et al.* Cell growth density modulates cancer cell vascular

invasion via Hippo pathway activity and CXCR2 signaling. *Oncogene* **34**, 5879–5889 (2015).

13. Oren, Y. *et al.* Cycling cancer persister cells arise from lineages with distinct programs. *Nature* **596**, 576–582 (2021).
14. Sun, X., Wu, L. F., Altschuler, S. J. & Hata, A. N. Targeting therapy-persistent residual disease. *Nat. Cancer* **5**, 1298–1304 (2024).
15. Li, T. *et al.* Variation in the life history strategy underlies functional diversity of tumors. *Natl. Sci. Rev.* **8**, nwaa124 (2021).
16. Mehta, A. & Stanger, B. Z. Lineage plasticity: The new cancer hallmark on the block. *Cancer Res.* **84**, 184–191 (2024).
17. Cook, D. P. & Vanderhyden, B. C. Transcriptional census of epithelial-mesenchymal plasticity in cancer. *Sci. Adv.* **8**, eabi7640 (2022).
18. Tammela, T. *et al.* A wnt-producing niche drives proliferative potential and progression in lung adenocarcinoma. *Nature* **545**, 355–359 (2017).
19. Wang, X. *et al.* Epithelial–mesenchymal plasticity in cancer: signaling pathways and therapeutic targets. *MedComm* **5**, e659 (2024).
20. Fabbri, L., Chakraborty, A., Robert, C. & Vagner, S. The plasticity of mRNA translation during cancer progression and therapy resistance. *Nat. Rev. Cancer* **21**, 558–577 (2021).
21. Langfelder, P. & Horvath, S. WGCNA: An R package for weighted correlation network analysis. *BMC Bioinformatics* **9**, 559 (2008).

675 22. Yang, L. *et al.* Targeting cancer stem cell pathways for cancer therapy.
676 *Signal Transduct. Target. Ther.* **5**, 8 (2020).
677 23. Frisardi, V., Canovi, S., Vaccaro, S. & Frazzi, R. The Significance of
678 Microenvironmental and Circulating Lactate in Breast Cancer. *Int. J. Mol.*
679 *Sci.* **24**, 15369 (2023).
680 24. Kotliar, D. *et al.* Identifying gene expression programs of cell-type identity
681 and cellular activity with single-cell RNA-seq. *eLife* **8**, e43803 (2019).
682 25. Yuan, S., Almagro, J. & Fuchs, E. Beyond genetics: Driving cancer with the
683 tumour microenvironment behind the wheel. *Nat. Rev. Cancer* **24**, 274–286
684 (2024).
685 26. Chaligne, R. *et al.* Epigenetic encoding, heritability and plasticity of glioma
686 transcriptional cell states. *Nat. Genet.* **53**, 1469–1479 (2021).
687 27. Zviran, A. *et al.* Deterministic somatic cell reprogramming involves
688 continuous transcriptional changes governed by myc and epigenetic-driven
689 modules. *Cell Stem Cell* **24**, 328-341.e9 (2019).
690 28. Zhu, Q. *et al.* Single cell multi-omics reveal intra-cell-line heterogeneity
691 across human cancer cell lines. *Nat. Commun.* **14**, 8170 (2023).
692 29. Maynard, A. *et al.* Therapy-induced evolution of human lung cancer
693 revealed by single-cell RNA sequencing. *Cell* **182**, 1232-1251.e22 (2020).
694 30. Nadalin, F. *et al.* Multi-omic lineage tracing predicts the transcriptional,
695 epigenetic and genetic determinants of cancer evolution. *Nat. Commun.* **15**,

7609 (2024).

31. Kussell, E. & Leibler, S. Phenotypic diversity, population growth, and information in fluctuating environments. *Science* **309**, 2075–2078 (2005).
32. Marrec, L. & Bank, C. Evolutionary rescue in a fluctuating environment: periodic versus quasi-periodic environmental changes. *Proc. R. Soc. B Biol. Sci.* **290**, 20230770 (2023).
33. Chevin, L.-M., Lande, R. & Mace, G. M. Adaptation, Plasticity, and Extinction in a Changing Environment: Towards a Predictive Theory. *PLoS Biol.* **8**, e1000357 (2010).
34. Pennekamp, F. *et al.* Biodiversity increases and decreases ecosystem stability. *Nature* **563**, 109–112 (2018).
35. Stajic, D., Bank, C. & Gordo, I. Adaptive Potential of Epigenetic Switching During Adaptation to Fluctuating Environments. *Genome Biol. Evol.* **14**, evac065 (2022).
36. Sharma, A. *et al.* Longitudinal single-cell RNA sequencing of patient-derived primary cells reveals drug-induced infidelity in stem cell hierarchy. *Nat. Commun.* **9**, 4931 (2018).
37. Maltas, J. *et al.* Drug dependence in cancer is exploitable by optimally constructed treatment holidays. *Nat. Ecol. Evol.* **8**, 147–162 (2023).
38. Schaff, D. L. *et al.* Pre-existing cell states predict resistance to multiple treatments. *Cell Genomics* **6**, 10.1016 (2026).

717 39. Chen, S., Zhou, Y., Chen, Y. & Gu, J. fastp: An ultra-fast all-in-one FASTQ
718 preprocessor. *Bioinformatics.* **34**, i884–i890 (2018).
719 40. Kim, D., Langmead, B. & Salzberg, S. L. HISAT: A fast spliced aligner with
720 low memory requirements. *Nat. Methods* **12**, 357–360 (2015).
721 41. Li, H. *et al.* The sequence alignment/map format and SAMtools.
722 *Bioinformatics.* **25**, 2078–2079 (2009).
723 42. Li, H. Aligning sequence reads, clone sequences and assembly contigs with
724 BWA-MEM. Preprint at https://doi.org/10.48550/arXiv.1303.3997 (2013).
725 43. Danecek, P. *et al.* The variant call format and VCFtools. *Bioinformatics.* **27**,
726 2156–2158 (2011).
727 44. Kumar, S. *et al.* MEGA12: Molecular evolutionary genetic analysis version
728 12 for adaptive and green computing. *Mol. Biol. Evol.* **41**, msae263 (2024).
729 45. Boeva, V. *et al.* Control-FREEC: A tool for assessing copy number and
730 allelic content using next-generation sequencing data. *Bioinformatics.* **28**,
731 423–425 (2012).
732 46. Langmead, B. & Salzberg, S. L. Fast gapped-read alignment with bowtie 2.
733 *Nat. Methods* **9**, 357–359 (2012).
734 47. Ramírez, F. *et al.* deepTools2: A next generation web server for deep-
735 sequencing data analysis. *Nucleic Acids Res.* **44**, W160–W165 (2016).
736 48. Zhang, Y. *et al.* Model-based analysis of ChIP-seq (MACS). *Genome Biol.*
737 **9**, R137 (2008).

49. Butler, A., Hoffman, P., Smibert, P., Papalexi, E. & Satija, R. Integrating single-cell transcriptomic data across different conditions, technologies, and species. *Nat. Biotechnol.* **36**, 411–420 (2018).

50. Yang, S. *et al.* Decontamination of ambient RNA in single-cell RNA-seq with DecontX. *Genome Biol.* **21**, 57 (2020).

51. McGinnis, C. S., Murrow, L. M. & Gartner, Z. J. DoubletFinder: Doublet Detection in Single-Cell RNA Sequencing Data Using Artificial Nearest Neighbors. *Cell Syst.* **8**, 329-337.e4 (2019).

Figures and legends

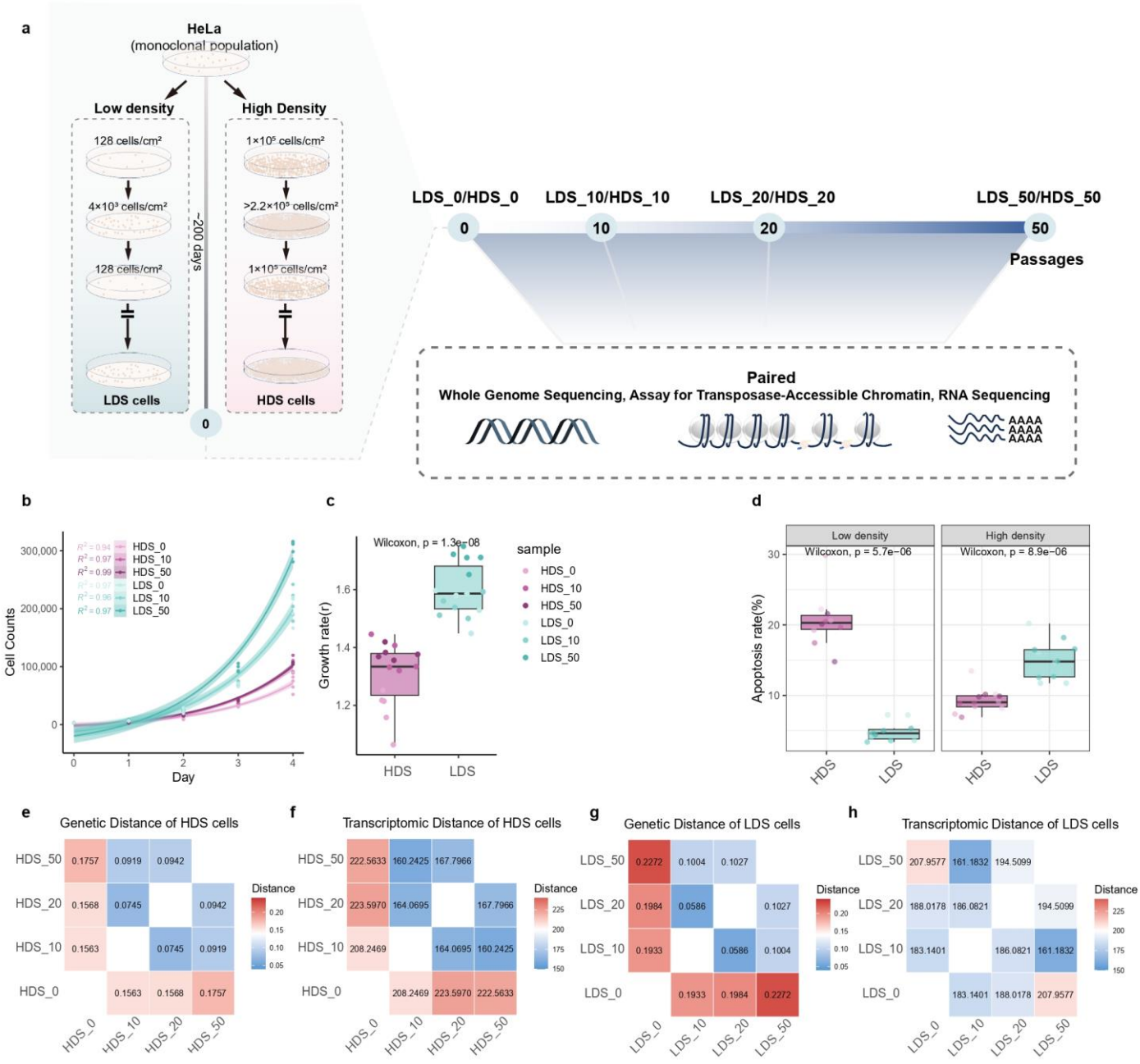


Figure 1. Establishment and long-term stability of a density-dependent experimental evolution system.

a, Schematic of the density-dependent experimental evolution system and sampling strategy. Monoclonal HeLa cells were subjected to long-term experimental evolution under persistently low-density or high-density culture conditions to generate low-density selected (LDS) and high-density selected (HDS) cell populations. Following the establishment of these density-adapted lineages, both populations were continuously propagated for an additional 50 passages to assess the long-term stability of the evolutionary system.

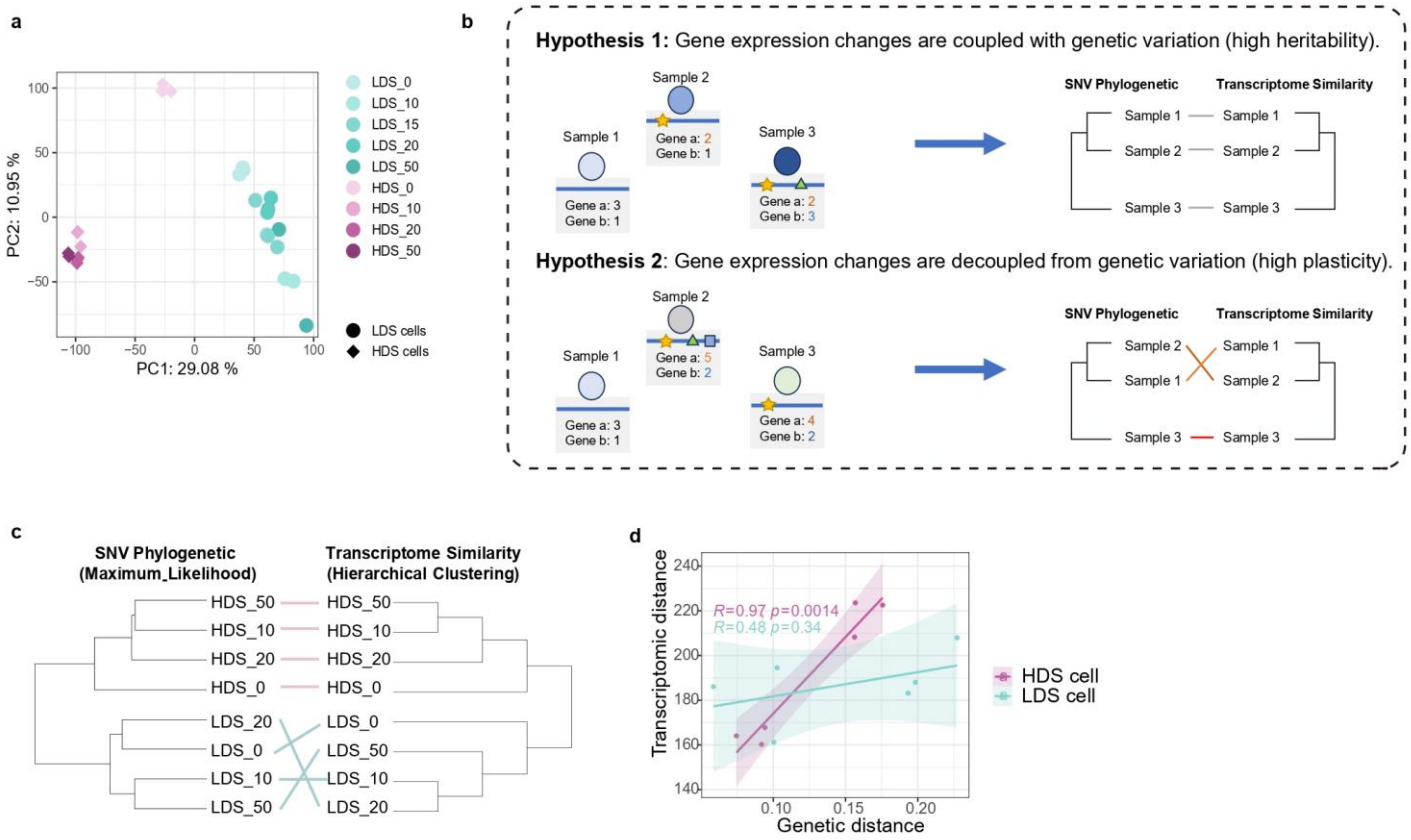
b, Logarithmic growth curves of LDS and HDS cells across passages. Cells were seeded at 3,000 cells per well and counted daily for four consecutive days.

c, Comparison of cell growth rates within LDS and HDS populations.

d, Density-dependent apoptosis across passages. Apoptosis was quantified in triplicate after cells were cultured for 3 days under low- and high-density conditions.

e-f, Genetic distances across passages, calculated as p-distance based on all identified single nucleotide variants (SNVs) within the LDS (e) and HDS (f) lineages.

g-h, Transcriptomic distances across passages, calculated as the Euclidean distance between normalized transcriptomes within the LDS (g) and HDS (h) lineages.



768 **Figure 2. Distinct mechanisms underlie transcriptomic divergence in LDS and**

769 **HDS cells.**

770 **a**, Principal component analysis (PCA) of genome-wide transcriptomes from LDS cells

771 at passages 0, 10, 15, 20, and 50 and HDS cells at passages 0, 10, 20, and 50,

772 illustrating the major sources of transcriptomic variation.

773 **b**, Schematic illustrating the relationship between genetic variation and transcriptomic

774 variation. Concordance between genetic and transcriptomic changes indicates high

775 heritability, whereas discordance suggests that transcriptomic variation is

776 predominantly driven by phenotypic plasticity.

777 **c**, Comparison of genetic and transcriptomic relationships across passages 0 to 50.

778 Genetic similarity was inferred from SNVs using maximum likelihood estimation,

779 whereas transcriptomic similarity was evaluated by hierarchical clustering. The
780 reduced concordance observed in LDS cells indicates increased phenotypic plasticity.
781 **d**, Pearson correlation between genetic and transcriptomic distances across passages.



Figure 3. Long-term evolution stabilizes distinct transcriptional programs in LDS and HDS cells.

a, EMT signature scores of LDS and HDS cells. Higher scores indicate a more mesenchymal-like phenotype.

b, Pathways consistently upregulated in LDS cells during long-term evolution.

c, Pathways consistently upregulated in HDS cells during long-term evolution.

d, e, Gene co-expression modules M1 and M2 showing strong associations with LDS (**d**) and HDS (**e**) cells across passages 0 to 50. *P* values were calculated using two-sided Wilcoxon tests.

f, g, Gene Ontology (GO) and Kyoto Encyclopedia of Genes and Genomes (KEGG) enrichment analyses of hub genes in modules M1 (**f**) and M2 (**g**). Hub genes were filtering by high-confidence protein–protein interactions (STRING, confidence>0.9) refined these to 248 and 84 core genes, respectively.

h–k, Single-cell transcriptomic characterization of representative LDS and HDS cells at passage 10, a stage at which the density-adapted phenotypes had become stably established.

h, UMAP visualization of LDS and HDS single cells at passage 10.

i, Identification of major cellular subclusters and their cell cycle phase distributions. Both LDS and HDS cells contained two major subclusters, whereas HDS cells exhibited greater cell cycle heterogeneity.

j, Consensus non-negative matrix factorization (cNMF) analysis identifying three gene expression programs.

804 **k**, Functional annotation of the three gene expression programs based on KEGG

805 pathway enrichment analysis of the top 200 weighted genes.

806

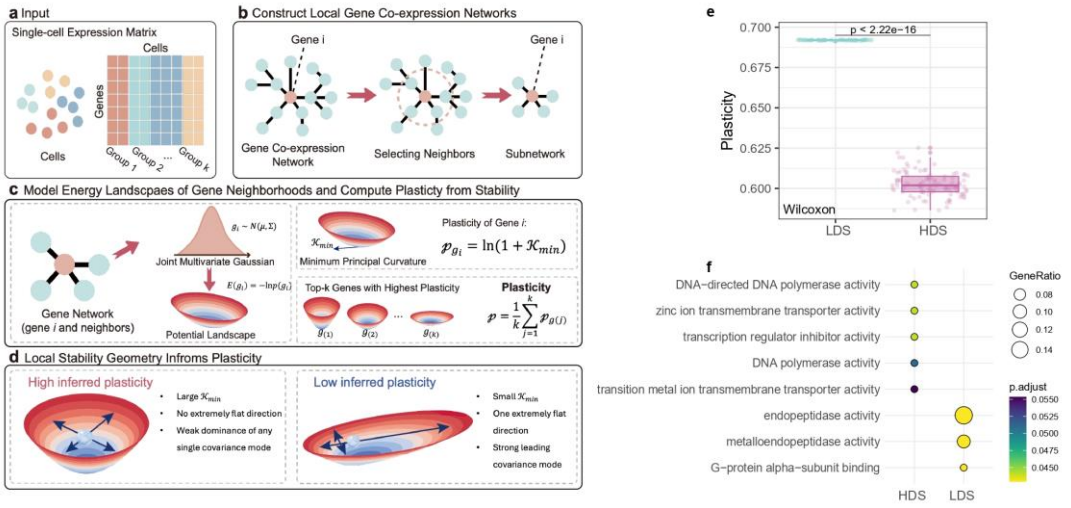
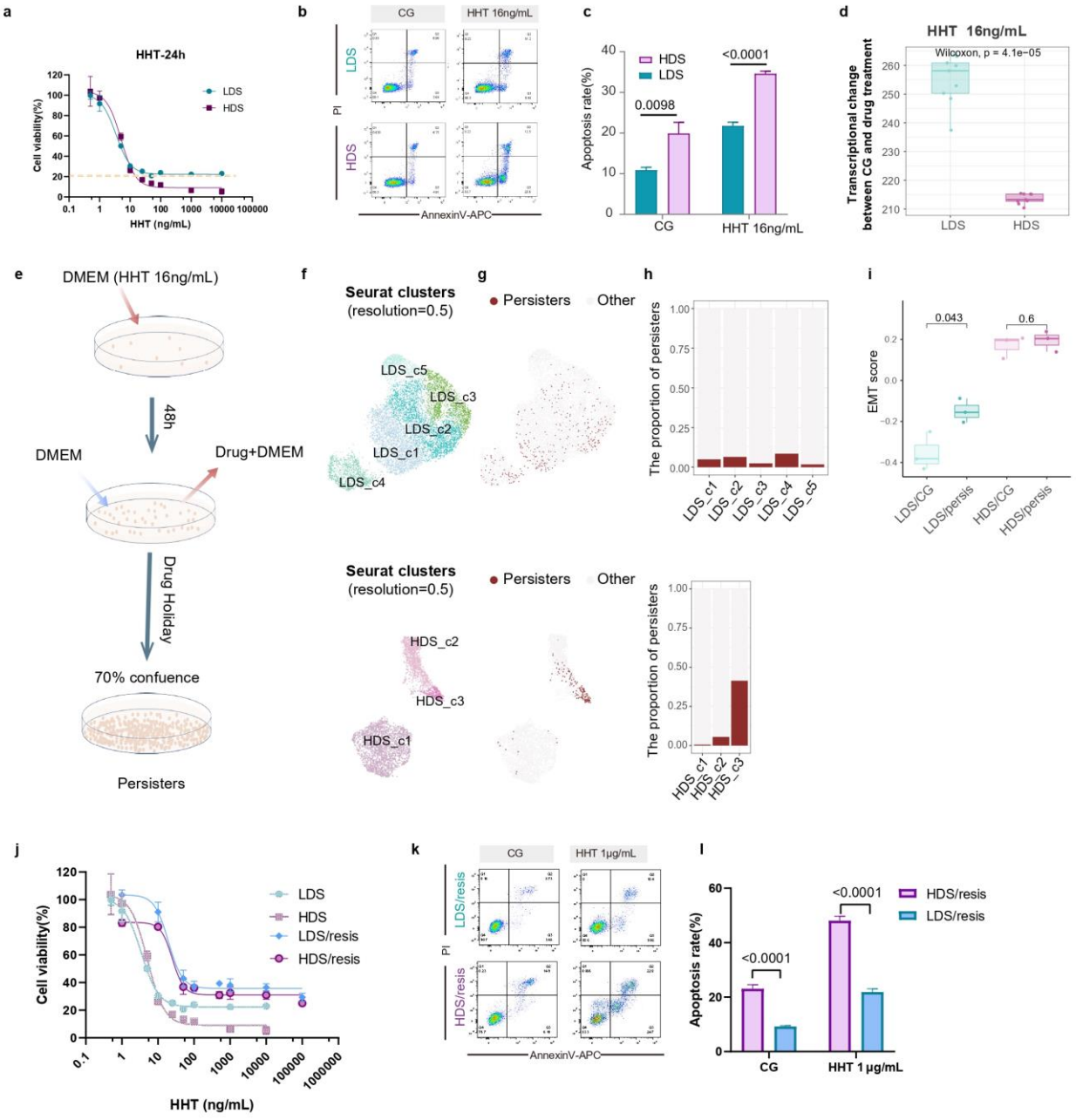


Figure 4. Energy landscape analysis quantitatively reveals greater regulatory flexibility in LDS cells.

a–d, Workflow for plasticity quantification based on local gene co-expression networks, including gene expression input (**a**), network construction (**b**), local energy landscape quantification (**c**), and calculation of the global plasticity score (**d**).

e, Global plasticity scores of LDS and HDS cells. Higher scores indicate greater transcriptional plasticity. *P* values were calculated using two-sided Wilcoxon tests.

f, GO enrichment analysis of hub genes from the 50 most plastic subnetworks.



816 **Figure 5. LDS cells exhibit broad-spectrum drug tolerance following both short-**

817 **term and long-term drug exposure.**

818 **a**, Cell viability of LDS and HDS cells after 24 h treatment with homoharringtonine

819 (HHT), measured using the CCK-8 assay.

b, Apoptosis of viable LDS and HDS cells following treatment with 16 ng/mL HHT, which reduced cell viability by approximately 80% to 90%.

c, Quantification of apoptosis rates. *P* values were calculated using two-sided T-tests.

d, Transcriptomic changes in LDS and HDS cells before and after HHT treatment. *P* values were calculated using two-sided Wilcoxon tests.

e–i, Characterization and inference of persister cells following HHT treatment in LDS and HDS populations.

e, Schematic of the persister isolation strategy. Cells were treated with HHT for 48 h and subsequently recovered in drug-free medium until reaching approximately 70% confluence before transcriptomic profiling (n = 3).

f, High-resolution reclustering of single-cell transcriptomes from LDS and HDS cells (resolution = 0.5).

g, Identification of inferred persister cells within the original single-cell populations. A persister signature was defined using the top 500 upregulated genes, and the top 5% of cells based on signature scores were classified as inferred persisters.

h, Distribution of inferred persisters across LDS and HDS cell subclusters.

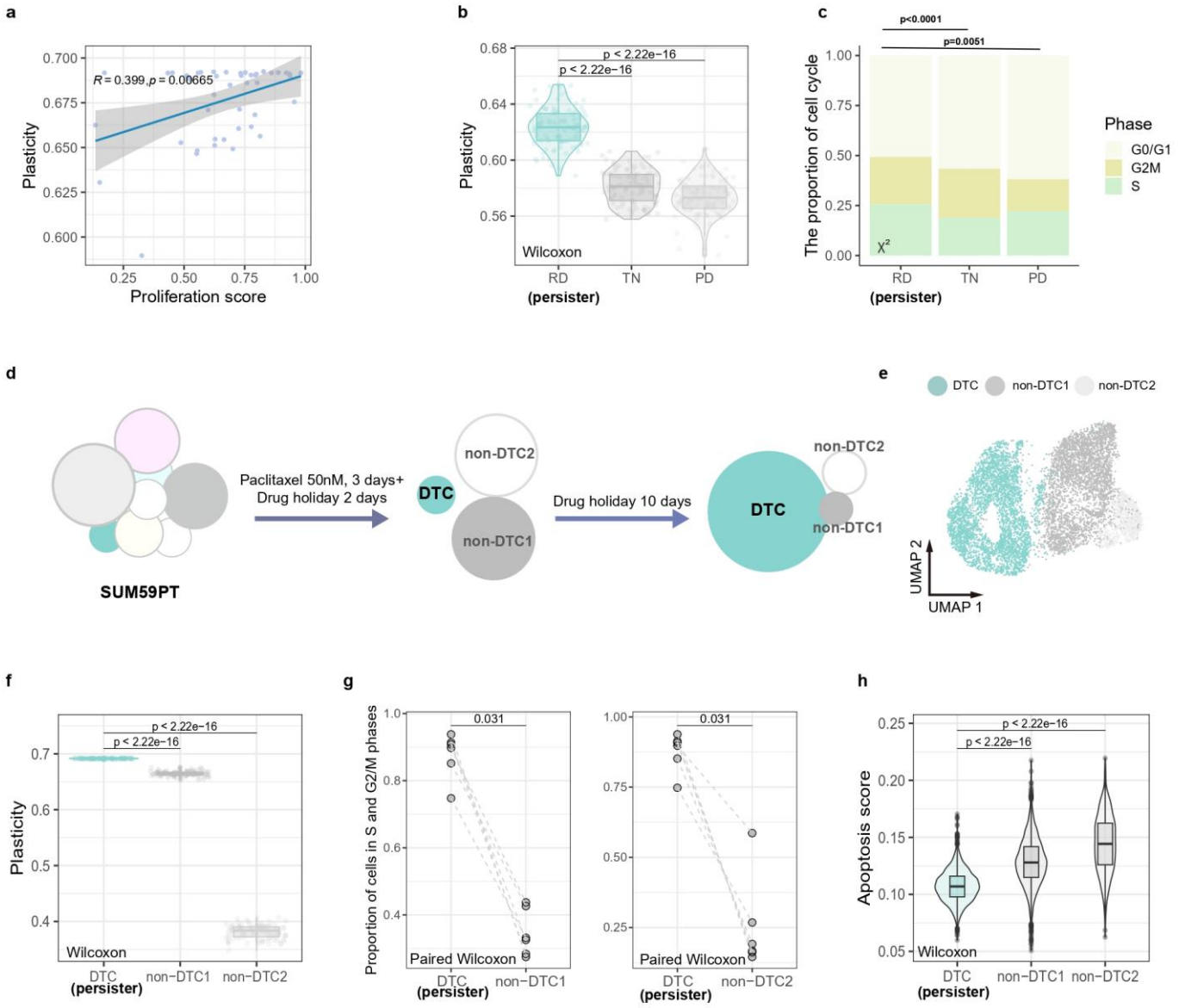
i, Comparison of EMT signature scores between control cells and their corresponding inferred persisters.

j–l, Phenotypic comparison of long-term HHT-resistant LDS and HDS cell lines generated by gradually increasing the HHT concentration from 16 ng/mL to 2,000 ng/mL.

j, Cell viability of HHT-resistant LDS and HDS cells following 24 h HHT treatment.

k, Apoptosis of viable HHT-resistant LDS and HDS cells following treatment with 1 μg/mL HHT, which reduced cell viability by approximately 80% to 90%.

l, Quantification of apoptosis rates. LDS-derived resistant cells exhibited significantly lower apoptosis under both standard culture conditions and HHT treatment.



846 **Figure 6. An LDS-like phenotype characterized by high plasticity and**

847 **proliferation confers enhanced drug tolerance across cancer cells.**

848 **a**, Pearson correlation between plasticity and proliferation scores across 42 cancer cell

849 lines comprising 45 samples. Proliferation was defined as the proportion of cells in

G2/S/M phase, whereas plasticity was quantified using local gene co-expression networks.

b, c, Quantification of plasticity (**b**) and proliferation (**c**) in a longitudinal lung cancer cohort comparing treatment-naïve (TN), residual disease (RD), and progressive disease (PD) samples. *P* values in **b** were calculated using two-sided Wilcoxon tests. *P* values in **c** were calculated using the chi-square test.

d–h, Longitudinal single-cell analysis during a drug holiday.

d, Experimental design. Cells were treated with 50 nM paclitaxel for 3 days, followed by a 12-day drug holiday. Single-cell transcriptomes were profiled at six time points. The dominant clone at day 12 was defined as the drug-tolerant clone (DTC).

e, UMAP visualization of all sampled cells.

f, Plasticity scores across cellular subpopulations.

g, Comparison of proliferation, measured as the proportion of cells in G2/S/M phase, between DTCs and the remaining subpopulations.

h, Apoptosis scores calculated using AUCell based on the MSigDB HALLMARK APOPTOSIS gene set. *P* values in **f–h** were calculated using two-sided Wilcoxon tests.

Supplementary Files

This is a list of supplementary files associated with this preprint. Click to download.

- SupplementaryInformation.pdf